IOPscience iopscience.iop.org

Home Search Collections Journals About Contact us My IOPscience

Deterministic radiative coupling between plasmonic nanoantennas and semiconducting nanowire quantum dots

This content has been downloaded from IOPscience. Please scroll down to see the full text.

2016 Nanotechnology 27 185201

(http://iopscience.iop.org/0957-4484/27/18/185201)

View the table of contents for this issue, or go to the journal homepage for more

Download details:

IP Address: 147.173.66.211
This content was downloaded on 23/05/2016 at 09:48

Please note that terms and conditions apply.

IOP Publishing Nanotechnology
Nanotechnology 27 (2016) 185201 (6pp) doi:10.1088/0957-4484/27/18/185201

Deterministic radiative coupling between plasmonic nanoantennas and semiconducting nanowire quantum dots

Mathieu Jeannin[1,2], Pamela Rueda-Fonseca[1,2,3], Edith Bellet-Amalric[1,3], Kuntheak Kheng[1,3] and Gilles Nogues[1,2]

[1] Univ. Grenoble Alpes, F-38000 Grenoble, France
[2] CNRS, Institut Néel, 'Nanophysique et semiconducteurs' group, F-38000 Grenoble, France
[3] CEA, INAC-SP2M, 'Nanophysique et semiconducteurs' group, F-38000 Grenoble, France

Received 27 November 2015, revised 8 February 2016
Accepted for publication 29 February 2016
Published 22 March 2016

Abstract

We report on the deterministic coupling between single semiconducting nanowire quantum dots emitting in visible and plasmonic Au nanoantennas. Both systems are separately and carefully characterized through micro-photoluminescence and cathodoluminescence. A two-step realignment process using cathodoluminescence allows for electron-beam lithography of Au antennas near individual nanowire quantum dots with a precision of 50 nm. A complete set of optical properties was measured before and after antenna fabrication. They evidence both an increase of the nanowire absorption, and an improvement of the quantum dot emission rate up to a factor of two in presence of the antenna.

S Online supplementary data available from stacks.iop.org/nano/27/185201/mmedia

Keywords: nanowire, nanoantenna, semiconductors, plasmonics, nanofabrication, cathodoluminescence

(Some figures may appear in colour only in the online journal)

1. Introduction

Recent progress in semiconductor growth research now allows for the fabrication of nanowire (NW) structures which are of great interest owing to their high crystalline quality, strain-free character and practical geometry. A key step towards the realization of nano-optical circuits and applications relies on the coupling of single NWs with other structures, like photonic crystal cavities [1] or plasmonic nanoantennas (NAs) [2–5] . To better use the advantages and the versatility of NWs, it is now necessary to adapt previous studies on self-assembled or colloidal quantum dots (QDs) to their NW counterparts. While numerous results have been obtained in the coupling of self-assembled [6–10] and colloidal [11, 12] QDs with plasmonic nanostructures, all the existing studies on control of the optical properties of nanowire quantum dots (NWQDs) rely on a photonic approach, using the nanowire itself as an antenna [13–15]. Following previous work in our group [8] on droplet epitaxy QDs, we show how combining cathodoluminescence (CL) with a standard e-beam lithography technique allows us to fabricate, at will, plasmonic NAs in the vicinity of II-VI NWQDs emitting around 620 nm. Both systems are initially fully characterized using CL for the antennas and micro-photoluminescence (μPL) as well as time-resolved spectroscopy for the emitters. Previous studies have made use of morphological criteria to detect nanoemitters, using scanning electron microscopy (SEM) or atomic force microscopy [7]. In contrast, our method has the advantage of allowing localization of embedded structures which are undetectable with the previous methods.

2. Nanowire quantum dot properties

Our nanoemitters are single (Cd,Mn)Te QDs (Mn fraction ≈5%) inserted inside ZnTe/(Zn,Mg)Te core/shell nanowires (figure 1(a)). The NWs are grown by molecular beam epitaxy

 © 2016 IOP Publishing Ltd Printed in the UK

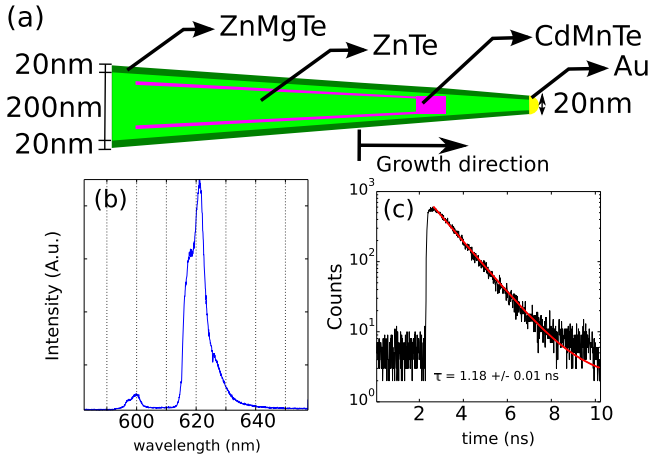

Figure 1. (a) Nanowire morphology: an Au droplet serves as a catalyst to grow a CdTe quantum dot inserted in a ZnTe conical nanowire. A lateral regrowth of ZnMgTe creates a shell around this core. (b) Typical μPL spectrum of a nanowire QD and (c) corresponding decay rate measurement, integrating a bandwidth of 10 nm around 622 nm. A monoexponential fit (red line) gives a lifetime $\tau = 1.18 \pm 0.01$ ns.

on a (111)B GaAs substrate covered by a 500 nm thick buffer layer of ZnTe [16, 17]. Dewetted gold droplets are used as catalysts, and temperature variations allow us to favor different growth mechanisms resulting in the final heterostructure. The core growth is both longitudinal and lateral, leading to the conical aspect of the nanowire, with a core diameter of 20 nm at the top to ≈200 nm at the base, and a 20 nm thick shell. The QD emission is measured by confocal μPL spectroscopy. It features a main emission peak around 620 nm, blue-shifted by 150 nm compared to the exciton transition in bulk CdTe [18] due to the confinement and the strain induced by the surrounding shell [19]. It is significantly broadened (FWHM 10 nm) by the presence of the magnetic Mn atoms creating a fluctuating magnetic field inside the QD, randomly shifting the exciton line in time by Zeeman effect [20] (figure 1(b)). Amongst all the studied NWs, the central emission wavelength ranges from 605 to 630 nm.

NWs are detached from their growth substrate and dispersed onto a host substrate for optical studies. The host is a Si substrate pre-patterned by optical lithography and dry etching to fabricate coarse localization marks. It is covered by a 100 nm thick Au layer deposited by e-gun evaporation and a 250 nm thick Al_2O_3 spacing layer by atomic layer deposition. The mirror and the spacer thickness are designed to give constructive interferences between the light directly emitted from the QD and the light reflected by the mirror in order to maximize luminescence collection. NWs are finally dispersed by mechanical contact between the host and growth substrates.

A first selection of NWs is performed using CL at 5 K [8, 16]. The luminescence from the QD is spectrally filtered and detected by an avalanche photodiode (APD). CL imaging of the emission profile at the QD luminescence wavelength is obtained for a set of NWs. To avoid spurious emission from excitons trapped in defects at the base of the NWs, we conserve only structures presenting a well-localized emission in the top half of the conical NW and having the typical spectral structure of figure 1(b). The selected QDs are then fully characterized by μPL spectroscopy at 5 K. The NWs are excited at 447 nm by a frequency doubled, ps-pulsed Ti:Sapphire laser. Time-resolved measurements are performed at very low pumping power, well below saturation of the QD, with a spectral integration bandwidth of 2 nm to ensure that we detect only the excitonic transition, resulting in a monoexponential time trace. They show decay times ranging from 0.2 to 1.18 ns (figure 1(c)). The average lifetime ($\tau = 0.68$ns) is about five times longer than for self-assembled CdTe/ZnTe QDs [21]. In addition, the emission from the QD is linearly polarized in a direction parallel to the NW axis in 70% of cases, and orthogonal in all the others. The average degree of linear polarization is 0.7 ± 0.2. These optical properties can be explained by the very small energy difference between the valence bands of CdTe and ZnTe [20]. The resulting nature of the hole ground state strongly depends on additional energy shifts induced by strain or QD aspect ratio [19, 22]. In our case, the orbital hole wavefunction is probably poorly confined inside the QD, resulting in low electron–hole wavefunction overlap and thus long radiative decay times. We note that the measured decay rate $1/\tau = \gamma_r + \gamma_{nr}$, where γ_r (resp. γ_{nr}) is the radiative (resp. non-radiative) decay rate, might be limited by non-radiative processes. Furthermore, a large variability from dot to dot strongly mixes the light- and heavy-hole bands, explaining the polarization results. This variability is not detrimental to our study as we compare a complete set of optical properties *on the one and same NW before and after antenna fabrication*.

3. Nanoantenna characterization

Au nanoantennas are fabricated on the host substrate, in a region empty of NWs. They consist in single rectangles of 70 nm fixed width, as sketched in figure 2(a). Their length L varies from 85 to 140 nm. They are fabricated by electron-beam lithography on a 200 nm thick Poly(methyl methacrylate) (PMMA) bi-layer resist, using PMMA with molecular weights of 50 kDa and 950 kDa to create a mechanical mask with the resist. 35 nm of Au is deposited on the sample by e-gun evaporation. N-methyl-2-pyrrolidone (NMP) lift-off with 80 °C heating is finally performed to remove the resist.

The antennas are characterized using CL at room temperature [23, 24]. The CL spectrum of each antenna is obtained by raster-scanning the electron beam over its surface. It presents a large peak at a fixed wavelength around 580 nm and a second resonance at lower energy. CL spectra for all the antennas are presented in figure 2(b), revealing that the second resonance red-shifts with increasing antenna length. We note that the optimization of the Al_2O_3 spacer thickness in order to increase the collected signal at 620 nm results in destructive interferences for the collected light in the 700 to 800 nm wavelength range, decreasing the detection contrast in this spectral region. Further information is obtained by imaging the plasmon local density of states (LDOS) [23]. It is

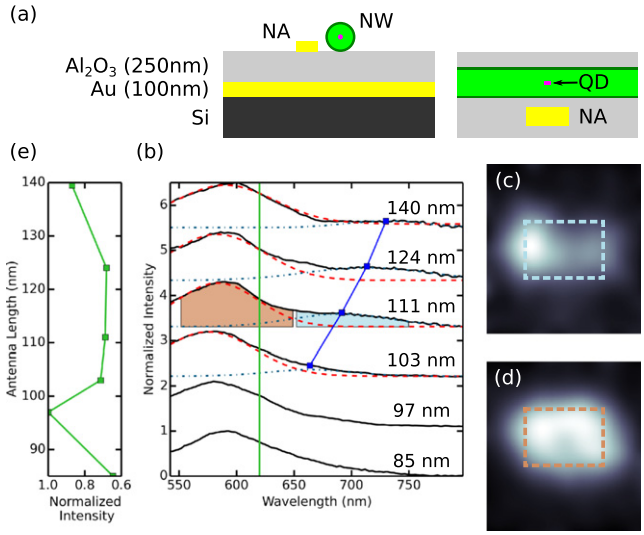

Figure 2. (a) Sketch of the NW–NA geometry (left: side view, right: top view), to scale. (b) Cathodoluminescence spectra of the rectangular nanoantennas, with Gaussian fits of the main component (red dashes) and the dipolar mode blue dashed-dotted line discussed in the text. The green line corresponds to (e). The blue line with squares indicates the fitted central wavelength of the dipolar resonance. The blue and brown shaded areas correspond to the integrated bandwidth in (c) (blue) and (d) (brown) respectively. (c) and (d) LDOS imaging of the 111 nm long antenna around 700 nm and 600 nm respectively, with 100 m spectral integration bandwidth. The blue and brown rectangles correspond to the antenna boundary. (e) Cut profile of the CL intensity along $\lambda_{QD} = 620$ nm (green solid line in (b)) showing an increase of the measured LDOS for an antenna length of 97 nm due to the onset of the dipolar mode.

reconstructed by slowly scanning the electron beam over the antenna and collecting the CL emission as a function of the beam position filtered in a 100 nm spectral window around the resonance energy on an APD. This spectral integration bandwidth is chosen to maximize the collected signal from the antenna. For $L \geqslant 110$ nm, it is smaller than the energy separation between two consecutive modes so that only a single resonance contributes to the LDOS image. The LDOS of the red-shifting resonance (figure 2(c)) clearly displays two lobes characteristic of a longitudinal dipolar mode. In this regime the antenna sustains a single radiating mode whose dispersion relation can be extracted from figure 2(b) (blue squares). On the contrary, the LDOS at 580 nm (figure 2(d)) shows no precise spatial structure at any length. We have fabricated NAs of different shapes, sizes and spacer thicknesses and observed that it is always present. The energy of its maximum depends only on the Al_2O_3 spacer thickness (see the supplementary material). We attribute this peak to the scattering by the NA of the continuum of surface plasmon polariton modes sustained by the $Au/Al_2O_3/air$ multilayer system. LDOS evaluation based on numerical calculations of the surface plasmon polariton dispersion relation [25] shows that at this energy a lot of lossy modes contribute to the signal. We note that in this study we use a 250 nm thick spacer for which no significant coupling occurs between the antenna and the metal film, which simply acts as a mirror to reflect emitted and scattered light towards the collection objective. To determine the relevant dimensions for enhancing emission processes at the QD wavelength, we plot a cut of figure 2(b) at $\lambda_{QD} = 620$ nm (green solid line, figure 2(e)). It predicts an increase in scattering efficiency for an antenna length around 95 nm due to the contribution of the dipolar mode. It also predicts an enhancement for lengths above 140 nm. This enhancement comes from the onset of a higher order mode theoretically predicted to appear at this length [25, 26]. We note however that for the target coupled NW–NA system, the presence of the very high refractive index nanowire ($n_{ZnTe} \approx 3$) in the near-field of the antenna significantly modifies its plasmonic properties. Hence a red-shift in the plasmon dispersion relation curve is expected, and the enhancement peaks observed in figure 2(e) will occur for smaller antenna lengths.

4. Hybrid NW–NA structures

4.1. Fabrication

Two examples of the target structure are shown in figures 3(d)–(e). Fine alignment marks are first fabricated around the chosen NWs using electron-beam lithography, metal evaporation and lift-off (figure 3(a)). We then record a SEM image (figure 3(b)) together with the CL intensity image at $\lambda_{QD} = 620$ nm (figure 3(c)). Both images are acquired after aligning the microscope beam using the fine alignment marks. Acquisition times are limited to a few seconds to limit mechanical and electrostatic drifts. We fit the QD emission peak with a bi-dimensional Gaussian profile and superimpose it to the corresponding SEM image. It allows us to precisely localize the QD inside the NW in the frame defined by the fine alignment marks. NAs are then fabricated with the same process as the previously characterized antennas. Before insulation of the resist, a final alignment step is performed onto the fine marks under the resist. The antennas have a fixed width $w = 70$ nm and a variable length L from 50 to 140 nm. This range is based on the previous CL results and takes into account the shift due to the presence of the NW. The antenna sides of length L are parallel to the measured polarization direction of the QD emission. We aim at having an antenna to NW gap equal to zero. SEM images reveal an average gap of 12 nm $\pm$ 50 nm, thus some antennas are on top of the NW. The final error of 50 nm has different sources. Alignment of the lithography setup has a typical error of 20 nm but is degraded in our case due to the poor contrast in the images of the fine alignment marks under the resist. We evaluate the error coming from the thermal, mechanical and electrostatic drifts during CL at low temperature to be 30 nm. We note that the NW core and shell are already thick (≈50 nm at the QD position). The resulting QD to antenna distance ranges from 50 to 110 nm. This distance is always large enough to prevent luminescence quenching, and the variations due to the positioning error only have a moderate effect on the NA to QD coupling [28].

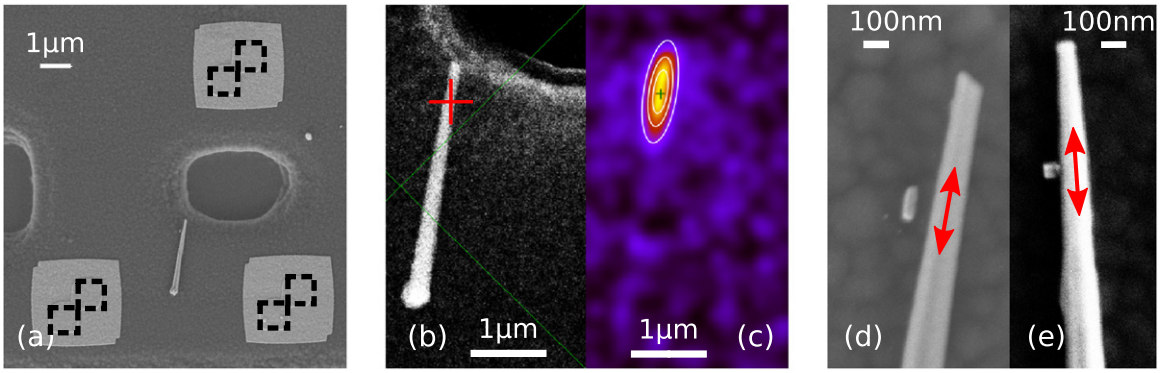

Figure 3. (a) Large field SEM image of the sample after antenna fabrication. The dashed lines indicate the position of the fine alignment marks which were exposed during the last alignment step and are hardly visible under the final Au layer. (b) Higher magnification SEM image of the NW after alignment with respect to the marks. (c) Filtered CL intensity at $\lambda_{QD} = 620$ nm at the same position and magnification. The red cross in (b) indicates the center of the bi-dimensional Gaussian fit. The white lines in (c) are contour lines of the fit. (d) SEM image of the resulting coupled NW–NA system, along with (e) another NW–NA system. The NW–NA gap is 60 nm in (d), while a point contact is achieved in (e). The red arrows indicates the polarization direction of the emitted light, which is ensured to be aligned with the antenna dipolar mode axis.

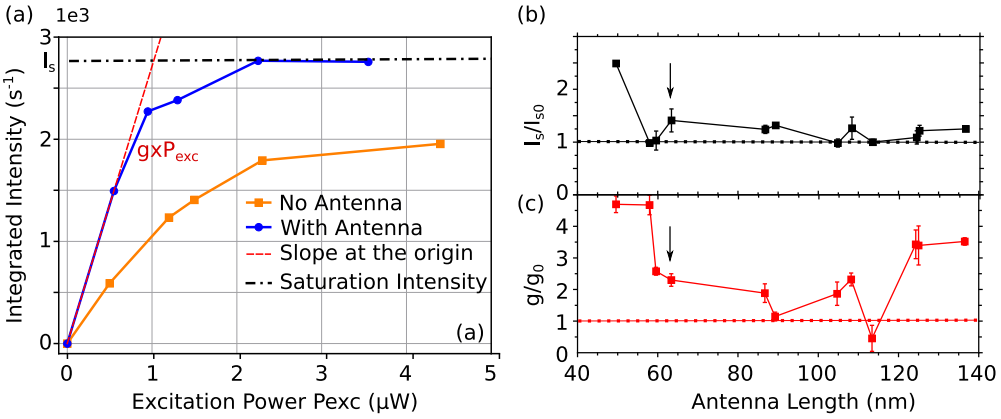

Figure 4. (a) Integrated μPL intensity for one NWQD as a function of excitation power before (orange square) and after (blue circle) nanoantenna fabrication. The NA is 63 nm long. Each data set is fitted with two components, a constant saturation intensity I_s, and a linear function of slope g describing the QD emission at low pumping power. I_s is determined by the last data point. g is determined between the first data point and the origin. (b) Saturation intensity I_s for the different NW–NA system divided by the corresponding value of the NW without antenna I_{s0} as a function of antenna length L. The error bars are given by the detection noise of the spectrometer. (c) Slope at the origin g for different NW–NA systems divided by the corresponding value of the NW without antenna g_0 as a function of L. The error bars are evaluated by comparing the slope at the origin and a linear regression between the first two data points and the origin. The arrows in (b) and (c) correspond to the NWQD presented in (a). The dotted line in each figure indicates a factor of 1.

4.2. Photoluminescence observations

The coupled QD–NA systems are characterized using μPL spectroscopy with a pulsed excitation laser at a wavelength of 447 nm. Figure 4(a) comparesthe integrated intensity emitted from a representative QD as a function of the exciting laser power P_{exc} before and after antenna fabrication for $L = 63$ nm. The PL intensity first increases with the excitation power and then saturates because of the complete occupation of the discrete excitonic state in the QD. For a same excitation power one clearly sees a much higher collected signal in presence of the NA. Similar measurements on other QDs (present on the same substrate) which have experienced the same process except the final antenna fabrication shows no change in their properties. Previous studies revealed modification of the luminescence collection by redirection of light by the antenna [5, 6, 8]. We have carried out Fourier plane microscopy by imaging the back focal plane of the microscope objective in the μPL setup (see supplementary material) to observe the radiation diagram of the NWQDs [29], and we did not observe a significant change in the radiation pattern after antenna fabrication. Clearly, the higher PL intensity we measure is not due to the redirection of light by the antennas. Additional information is provided by measurements of the exciton lifetime before (τ_0) and after (τ_{NA}) antenna fabrication under the same excitation conditions. We observe no significant change, with an average ratio $\tau_{NA}/\tau_0 = 1.1 \pm 0.2$ (see supplementary materials).

To better analyze the effect of the antennas, we evaluate the saturation intensity I_s at high excitation power, and the slope at the origin g of the power-dependent μPL curve. The

ratio of I_s before and after antenna fabrication is plotted as a function of antenna length in figure 4(b), showing a net increase after NA fabrication. As shown in figure 4(c), we also observe a greater increase in the slope g after NA fabrication.

4.3. Discussion

Assuming that we only detect the excitonic transition and considering that the nanowire excitation is done with a pulsed laser, the saturation intensity I_s is equal to $f \times \gamma_r/(\gamma_r + \gamma_{nr}) \times \alpha_{coll}$, where f is the laser repetition rate, $Y = \gamma_r/(\gamma_r + \gamma_{nr})$ is the quantum yield and α_{coll} is the fraction of the emitted power collected by the microscope objective. As we measure no change in the radiation diagram after NA fabrication, it is reasonable to assume that α_{coll} is unaffected. As a consequence the enhancement observed in figure 4(b) is directly related to an increase in the quantum yield Y. This enhancement is found to be moderate for antennas with a length greater than 60 nm but stronger for the smallest antennas, up to a factor of 2.5. As expected from section 3, this occurs for antennas that are shorter than the determined resonant length from figure 2(e). Moreover since the QD response at saturation is independent of the excitation power, the change of I_s after antenna fabrication is not due to an increase of the absorption inside the NW.

Nevertheless, CL spectra of the NAs at $\lambda_{exc} = 447$ nm show that there is still a measurable LDOS at this energy that can modify the absorption of the excitation laser inside the NW (see supplementary material). The main contribution to this LDOS comes from the fixed resonance observed in figure 2 and does not depend on the antenna length. The change of the absorption can be retrieved by analyzing the slope at the origin g. In the limit of low excitation regime, g is expected to be proportional to $Y \times \alpha_{abs} \times \alpha_{coll}$, where α_{abs} is the fraction of power absorbed in the NW. As α_{coll} remains unchanged after NA fabrication, the ratio $(g/g_0)/(I_s/I_{s0})$ directly gives the change in α_{abs}. The comparison of figures 4(b) and (c) shows that the absorption in the NW is enhanced by a factor of 2.2 ± 1.1 over the whole antenna length range. Further illustration of the respective changes in I_s and g are presented in the supplementary material with two other power-dependent μPL curves. Our main conclusion is that, for the shorter antenna lengths, enhanced NW absorption and improvement of the quantum yield contribute equally to the four-fold increase of g that we observe.

Finally, lifetime measurements show that there is no change of the total decay rate $\gamma_r + \gamma_{nr}$. This is an indication that the total decay rate is dominated by the non-radiative term γ_{nr} and is moderately affected by a change in γ_r. Therefore, the observed increase in Y is essentially due to an increase of the QD radiative rate γ_r because of coupling to the NA.

5. Conclusion

In conclusion, we demonstrated deterministic coupling between single semiconducting nanowire quantum dots and plasmonic nanoantennas using CL and electron-beam lithography with a precision of 50 nm. Our method has the advantage of relying only on the luminescence of the emitters for their precise localization. It also grants full characterization of individual nanoemitters and antennas. CL spectroscopy and LDOS imaging of individual NAs is demonstrated as a powerful technique to experimentally determine antenna parameters for the fabrication of coupled plasmonic-semiconductor emitters. Furthermore, we demonstrate two effects of the NAs on the QDs: an absorption enhancement by a factor of 2, and a light emission enhancement due to radiative coupling to the antenna up to a factor of 2.5 in a spectral region of high plasmonic loss, extending the control of light emission from semiconducting nanostructures towards the visible spectral region. The effect could be greatly increased for a smaller QD–antenna distance, i.e. using a thinner NW shell. Implementation of the method is a crucial step towards fabricating more complex and versatile coupled structures. It can be applied to all kinds of nanoemitters, aiming at controlling their optical properties such as their polarization response [4, 10] or emission diagram [6, 9].

Acknowledgments

We acknowledge the help of Institut Néel technical support teams Nanofab (clean room) and optical engineering (CL, Fabrice Donatini). This work was supported by the French National Research Agency (project Magwires, ANR-11-BS10-013 and Labex LANEF du Programme d'Investissements d'Avenir ANR-10-LABX-51-01).

References

[1] Birowosuto M D, Yokoo A, Zhang G, Tateno K, Kuramochi E, Taniyama H, Takiguchi M and Notomi M 2014 *Nat. Mater.* **13** 279–85
[2] Ozel T, Bourret G R, Schmucker A L, Brown K A and Mirkin C A 2013 *Adv. Mater.* **25** 4515–20
[3] Casadei A *et al* 2014 *Nano Lett.* **14** 2271–8
[4] Casadei A, Llado E A, Amaduzzi F, Russo-Averchi E, Rüffer D, Heiss M, Negro L D and Morral A F 2015 *Sci. Rep.* **5** 7651
[5] Ramezani M, Casadei A, Grzela G, Matteini F, Tütüncüoglu G, Rüffer D, Fontcuberta I M A and Gómez Rivas J 2015 *Nano Lett.* **15** 4889–95
[6] Curto A G, Volpe G, Taminiau T H, Kreuzer M P, Quidant R and van Hulst N F 2010 *Science* **329** 930–3
[7] Pfeiffer M, Lindfors K, Wolpert C, Atkinson P, Benyoucef M, Rastelli A, Schmidt O G, Giessen H and Lippitz M 2010 *Nano Lett.* **10** 4555–8
[8] Nogues G, Merotto Q, Bachelier G, Hye Lee E and Dong Song J 2013 *Appl. Phys. Lett.* **102** 231112
[9] Belacel C *et al* 2013 *Nano Lett.* **13** 1516–21
[10] Kukushkin V I, Mukhametzhanov I M, Kukushkin I V, Kulakovskii V D, Sedova I V, Sorokin S V, Toropov A A, Ivanov S V and Sobolev A S 2014 *Phys. Rev.* B **90** 235313

[11] Curto A G, Taminiau T H, Volpe G, Kreuzer M P, Quidant R and van Hulst N F 2013 *Nat Commun.* **4** 1750
[12] Hoang T B, Akselrod G M and Mikkelsen M H 2016 *Nano Lett.* **16** 270–5
[13] Claudon J, Bleuse J, Malik N S, Bazin M, Jaffrennou P, Gregersen N, Sauvan C, Lalanne P and Gérard J M 2009 *Nat. Photonics* **3** 116–116
[14] Munsch M, Claudon J, Bleuse J, Malik N S, Dupuy E, Gérard J M, Chen Y, Gregersen N and Mørk J 2012 *Phys. Rev. Lett.* **108** 077405
[15] Cremel T, Elouneg-Jamroz M, Bellet-Amalric E, Cagnon L, Tatarenko S and Kheng K 2014 *Phys. Status Solidi* C **11** 1263–6
[16] Artioli A A *et al* 2013 *Appl. Phys. Lett.* **103** 222106
[17] Rueda-Fonseca P *et al* 2014 *Nano Lett.* **14** 1877–83
[18] Horodyský P and Hlídek P 2005 *Phys. Status Solidi* **243** 494–501
[19] Ferrand D and Cibert J 2014 *Eur. Phys. J. Appl. Phys.* **67** 30403
[20] Stepanov P S 2013 Magneto-optical spectroscopy of magnetic semiconductor nanostructures *PhD Thesis* https://tel.archives-ouvertes.fr/tel-00994939 Université de Grenoble
[21] Man M T and Lee H S 2015 *Sci. Rep.* **5** 8267
[22] Zieliński M 2013 *Phys. Rev.* B **88** 115424
[23] García de Abajo F J 2010 *Rev. Mod. Phys.* **82** 209–75
[24] Vesseur E J R, de Waele R, Kuttge M and Polman A 2007 *Nano Lett.* **7** 2843–6
[25] Davis T 2009 *Opt. Commun.* **282** 135–40
[26] Filter R, Qi J, Rockstuhl C and Lederer F 2012 *Phys. Rev.* B **85** 125429
[27] Anger P, Bharadwaj P and Novotny L 2006 *Phys. Rev. Lett.* **96** 113002
[28] Grzela G, Paniagua-Domínguez R, Barten T, Fontana Y, Sánchez-Gil J A and Gómez Rivas J 2012 *Nano Lett.* **12** 5481–6